Morphological cell profiling of SARS-CoV-2 infection identifies drug repurposing candidates for COVID-19

Carmen Mirabelli[a,1], Jesse W. Wotring[b,c,1], Charles J. Zhang[b,c,2], Sean M. McCarty[b,2], Reid Fursmidt[c,d,2], Carla D. Pretto[c], Yuanyuan Qiao[e,f], Yuping Zhang[e,f], Tristan Frum[g], Namrata S. Kadambi[c], Anya T. Amin[c], Teresa R. O'Meara[a], Jason R. Spence[c,g], Jessie Huang[h,i,j], Konstantinos D. Alysandratos[h,i,j], Darrell N. Kotton[h,i,j], Samuel K. Handelman[c,d], Christiane E. Wobus[a], Kevin J. Weatherwax[d,k,l], George A. Mashour[d,k,m], Matthew J. O'Meara[n,3], Arul M. Chinnaiyan[e,f,o,p,q,3,4], and Jonathan Z. Sexton[b,c,d,k,3,4]

[a]Department of Microbiology and Immunology, University of Michigan Medical School, Ann Arbor, MI 48109; [b]Department of Medicinal Chemistry, College of Pharmacy, University of Michigan, Ann Arbor, MI 48109; [c]Department of Internal Medicine, Division of Gastroenterology and Hepatology, Michigan Medicine at the University of Michigan, Ann Arbor, MI 48109; [d]Center for Drug Repurposing, University of Michigan, Ann Arbor, MI 48109; [e]Michigan Center for Translational Pathology, University of Michigan, Ann Arbor, MI 48109; [f]Department of Pathology, University of Michigan, Ann Arbor, MI 48109; [g]Department of Cell and Developmental Biology, University of Michigan, Ann Arbor, MI 48109; [h]Center for Regenerative Medicine, Boston University and Boston Medical Center, Boston, MA 02118; [i]Pulmonary Center, Boston University School of Medicine, Boston, MA 02118; [j]Department of Medicine, Boston University School of Medicine, Boston, MA 02118; [k]Michigan Institute for Clinical and Health Research, University of Michigan, Ann Arbor, MI 48109; [l]College of Pharmacy, University of Michigan, Ann Arbor, MI 48109; [m]Department of Anesthesiology, University of Michigan, Ann Arbor, MI 48109; [n]Department of Computational Medicine and Bioinformatics, University of Michigan, Ann Arbor, MI 48109; [o]Rogel Cancer Center, University of Michigan, Ann Arbor, MI 48109; [p]HHMI, University of Michigan, Ann Arbor, MI 48109; and [q]Department of Urology, University of Michigan, Ann Arbor, MI 48109

Contributed by Arul M. Chinnaiyan, July 9, 2021 (sent for review March 25, 2021; reviewed by Matthew L. Albert and Sumit Chanda)

The global spread of the severe acute respiratory syndrome coronavirus 2 (SARS-CoV-2), and the associated disease COVID-19, requires therapeutic interventions that can be rapidly identified and translated to clinical care. Traditional drug discovery methods have a >90% failure rate and can take 10 to 15 y from target identification to clinical use. In contrast, drug repurposing can significantly accelerate translation. We developed a quantitative high-throughput screen to identify efficacious agents against SARS-CoV-2. From a library of 1,425 US Food and Drug Administration (FDA)-approved compounds and clinical candidates, we identified 17 hits that inhibited SARS-CoV-2 infection and analyzed their antiviral activity across multiple cell lines, including lymph node carcinoma of the prostate (LNCaP) cells and a physiologically relevant model of alveolar epithelial type 2 cells (iAEC2s). Additionally, we found that inhibitors of the Ras/Raf/MEK/ERK signaling pathway exacerbate SARS-CoV-2 infection in vitro. Notably, we discovered that lactoferrin, a glycoprotein found in secretory fluids including mammalian milk, inhibits SARS-CoV-2 infection in the nanomolar range in all cell models with multiple modes of action, including blockage of virus attachment to cellular heparan sulfate and enhancement of interferon responses. Given its safety profile, lactoferrin is a readily translatable therapeutic option for the management of COVID-19.

SARS-CoV-2 | drug repurposing screening | COVID-19 | lactoferrin

Severe acute respiratory syndrome coronavirus 2 (SARS-CoV-2) is an enveloped, positive-sense, single-stranded RNA *betacoronavirus* that emerged in Wuhan, China in November 2019 and rapidly developed into a global pandemic. The associated disease, COVID-19, manifests with an array of symptoms, ranging from flu-like illness and gastrointestinal distress (1, 2) to acute respiratory distress syndrome, heart arrhythmias, strokes, and death (3, 4). Recently, the US Food and Drug Administration (FDA) issued emergency approval of remdesivir, a nucleoside inhibitor prodrug developed for Ebola virus treatment (5). Although large-scale vaccination is ongoing worldwide, the need for safe, readily available antivirals is still a clinical priority. An antiviral compound that curbs infection and reduces COVID-19 symptoms would be highly useful to control local outbreaks or for home-based management, to protect immunocompromised patients for whom vaccination strategies are not suitable, and to slow the spread of variants of concern that could escape vaccine neutralization.

Repurposing of FDA-approved drugs is a promising strategy for identifying rapidly deployable treatments for COVID-19. Benefits of repurposing include known safety profiles, robust supply chains, and a short time frame necessary for development (6). Additionally, approved drugs can serve as chemical probes to understand the biology of viral infection and inform on the molecular targets/pathways that influence SARS-CoV-2 infection. To date, several drug repurposing screening efforts have been reported in various cell systems including nonhuman primate VeroE6 (7), Huh7.5 (8), and Caco-2 cells (9) with a significant overlap in reported drugs but with wide-ranging potencies. Here, we developed a pipeline for quantitative high-throughput image-based screening of SARS-CoV-2 infection that led to the identification of several FDA-approved drugs and clinical candidates with previously unreported in vitro antiviral activity. We also determined that inhibitors of the Ras/Raf/MEK/ERK signaling pathway exhibited proviral activity in Huh7 cells. Mechanism of action studies of lactoferrin, the most promising hit, identified that it inhibits viral attachment, enhances antiviral host cell responses, and potentiates the effects of remdesivir.

Significance

Since its emergence in China in December 2019, SARS-CoV-2 has caused a global pandemic. Repurposing of FDA-approved drugs is a promising strategy for identifying rapidly deployable treatments for COVID-19. Herein, we developed a pipeline for quantitative, high-throughput, image-based screening of SARS-CoV-2 infection in human cells that led to the identification of several FDA-approved drugs and clinical candidates with in vitro antiviral activity.

Author contributions: C.M., J.W.W., C.J.Z., S.M.M., R.F., C.D.P., T.F., N.S.K., A.T.A., C.E.W., M.J.O., A.M.C., and J.Z.S. designed research; C.M., J.W.W., C.J.Z., C.D.P., Y.Q., Y.Z., and G.A.M. performed research; J.R.S., J.H., K.D.A., and D.N.K. contributed new reagents/analytic tools; C.M., J.W.W., C.J.Z., S.M.M., R.F., Y.Q., Y.Z., S.K.H., M.J.O., and J.Z.S. analyzed data; and C.M., J.W.W., C.J.Z., T.R.O., C.E.W., K.J.W., G.A.M., M.J.O., A.M.C., and J.Z.S. wrote the paper.

Reviewers: M.L.A., insitro; and S.C., Sanford Burnham Prebys Medical Discovery Institute.

The authors declare no competing interest.

[1]C.M. and J.W.W. contributed equally to this work.

[2]C.J.Z., S.M.M., and R.F. contributed equally to this work.

[3]M.J.O., A.M.C, and J.Z.S. contributed equally to this work.

[4]To whom correspondence may be addressed. Email: arul@umich.edu or jzsexton@med.umich.edu.

This article contains supporting information online at https://www.pnas.org/lookup/suppl/doi:10.1073/pnas.2105815118/-/DCSupplemental.

Published August 19, 2021.

Results

To determine the optimal cell line and assay timing for antiviral drug screening, we assessed SARS-CoV-2 infectivity in Vero E6 (African green monkey kidney cells), Caco-2 (human colon adenocarcinoma cells), Huh7 (human hepatocyte carcinoma cells), and LNCaP (human prostate adenocarcinoma cells). Viral growth kinetics at a multiplicity of infection (MOI) of 0.2 revealed that each cell line supported viral infection with peak viral titers at 24 h post infection (h p.i.) in VeroE6, at 48 h p.i. in Huh7 and Caco-2 cells, and 72 h p.i. in LNCaP (*SI Appendix*, Fig. S1*A*). The Huh7 cell line was selected for drug screening because of its human origin and it produced the maximum percentage of infected cells (~20%) at 48 h p.i. at a MOI of 0.2, while Caco-2 and LNCaP required higher MOI to show the same infection rates (*SI Appendix*, Fig. S1*B*). Huh7 also exhibited superior signal to background for N-protein staining, and viral infection was detectable at an MOI of as low as 0.004 at 48 h p.i. (*SI Appendix*, Fig. S1*C*).

Cell Morphological Profiling of SARS-CoV-2–Infected Cells. To gain insight into cellular features that are perturbed upon infection, a cell painting style morphological profiling assay was developed in 384-well plates. A multiplexed fluorescent dye set labeling the SARS-CoV-2 nucleocapsid protein (N), nuclei (Hoechst 33342), neutral lipids (HCS LipidTox Green), and cytoplasm (HCS CellMask Orange) was used to capture a wide variety of cellular features relevant to viral infectivity, including nuclear morphology, nuclear texture, and cytoplasmic and cytoskeletal features. Cell-level features of infected and uninfected cells were measured using a CellProfiler (10) image analysis pipeline. We observed several prominent features associated with SARS-CoV-2 infection, including the formation of syncytia, cytoplasmic protrusions, multiple cell shapes, and positive/negative N-protein staining within the nucleus. Fig. 1*A* shows multiplexed images of infected and uninfected wells and resulting identification/segmentation of infected cells. To systematically explore the morphologies of infected cells, features were dimensionally reduced via the nonlinear uniform manifold approximation and projection (UMAP). The analysis showed five regions of interest (ROIs) (Fig. 1*B*) with selected phenotypes. These phenotypes included rounded up cells with intense N staining overlapping with the nuclei (ROI-I), diffuse N staining in the cytoplasm of cells with normal shape and size (ROI-II), and cells with abnormal cytoplasmic protrusions containing punctate N staining (ROI-III) or diffused N staining (ROI-IV). Most infected cells, however, clustered in syncytia (ROI-V), suggesting that infection in Huh7 propagates primarily through cell-to-cell fusion. Fig. 1*C* shows split violin plots for prominent features that are perturbed in infected vs. uninfected cells. Inspection of the spatial arrangement of the morphologic classes of infected cell suggests a trajectory that starts with punctate/dim N-protein staining in individual cells that progresses to cells with N-protein–positive filapodia and associated membrane blebbing that enables cell-to-cell infection process (11). As the trajectory increases, N-protein staining increases (ROI-II) and then is visible in the nucleus, a process presumably mediated by multiple NLS sequences (ROI-I) (12). At this point, mature infected (ROI-I) cells are surrounded by early punctate infected cells (ROI-III) that represent the second round of infected cells. These clusters ultimately converge to form large syncytia and remain stable as Huh7 cells do not progress to exhibiting a cytopathic effect. Viral staining, cytoplasmic intensity (CellMask), and nuclear texture all increase in infected cells. In addition, the neutral lipid droplet content increases and the radial distribution of the lipid droplets shifts outward from the nucleus toward the plasma membrane. Increased lipid accumulation has been observed previously in hepatitis C virus-infected Huh7 cells (13). The CellMask intensity is increased in infected cells due to the prevalence of syncytia where the disappearance of cell boundaries increases staining intensity at the cell edge. Collectively, our analysis identifies specific features that are characteristic of SARS-CoV-2–infected Huh7 cells.

Identification of FDA-Approved Drugs with Antiviral Activity Against SARS-CoV-2. To identify compounds with antiviral activity against SARS-CoV-2, we tested a library of 1,425 FDA-approved compounds and rationally included clinical candidates (*SI Appendix*) in Huh7 cells in quantitative high-throughput screening (qHTS) at five concentrations (50, 250, 500, 1,000, and 2,000 nM). Compounds were selected for inclusion if they were FDA-approved and readily commercially available, and chemical probes previously reported to have any general antiviral activity. Compounds were assessed for their antiviral activity (shown schematically in Fig. 2*A*) using a CellProfiler (10) image analysis pipeline to 1) identify infected objects in the N protein image (from a single cell to large syncytia), 2) measure their morphologic features, and then 3) tabulate how many nuclei reside within the infected objects to calculate the total percentage of infected cells per well. To increase the likelihood of identifying true actives and decrease the false-negative rate of the assay, a liberal selection criterion was employed to choose drugs for follow-up studies (see *Methods* and Fig. 2*A*). One hundred thirty-two drugs were selected from qHTS screening or by known activity against SARS, MERS, or SARS-CoV-2 and carried forward for triplicate dose–response confirmation. Ultimately, 17 dose-responsive compounds were confirmed with IC_{50} values of less than 1 μM (Fig. 2*B* and Table 1). The remaining compounds either lacked efficacy, exhibited cytotoxicity (e.g., digoxin), or were efficacious only at concentrations above 1 μM (e.g., hydroxychloroquine, chloroquine) and were thus not prioritized for follow-up. Collectively, the 17 identified hits could be stratified by compound class as ion channel modulators (amiodarone, verapamil, clofazimine, and S1RA), nucleosides/DNA binders (remdesivir, entecavir, niclosamide, and thioguanine), kinase inhibitors (bosutinib, fedratinib, and gilterinib), and others (Table 1).

Hit Validation in Caco-2, LNCaP, Vero E6, and an Induced Pluripotent Stem Cell–Derived Model of Alveolar Epithelial Cells, the iAEC2. To evaluate the translatability of the 17 hits from Huh7 cells in other cell systems, we confirmed activity in LNCaP, Caco-2, and Vero E6 cell lines and in physiologically relevant induced pluripotent stem cell (iPSC)-derived alveolar epithelial type 2 cells (iAEC2s) (16). Antiviral activities across the cell systems are shown in Table 1. iAEC2s were used as a biomimetic model of the human bronchial epithelium that is involved in COVID-19 pathogenesis (17). iAEC2s are permissive to SARS-CoV-2 infection, exhibiting 10–20% N protein-positive cells at MOI of 0.2 and 50–60% positivity at MOI of 10. Upon infection, we observed long tubular protrusions that costained with viral N protein (Fig. 3*A*). Additionally, unlike the Huh7 model, the vast majority of infected iAEC2 cells were not present in viral syncytia, suggesting that cell-to-cell spread by cell fusion is limited in this model. Nine out of the 17 hits—amiodarone, lomitapide, ipratropium bromide, gilteritinib, fedratinib, clofazimine, remdesivir, S1RA, and bovine lactoferrin—showed dose-responsive antiviral activity against SARS-CoV-2 in iAECs (Table 1). Remarkably, even at a high MOI of 10, bovine lactoferrin, human lactoferrin, S1RA, and remdesivir retained antiviral activity, reflecting the strong efficacy of these compounds in virus-saturated infection conditions (Fig. 3*B*). Six compounds (amiodarone, ipatropium bromide, lactoferrin, lomitapide, remdesivir, and Z-FA-FMK) maintained efficacy across all tested cell systems (Table 1), suggesting the targets are conserved across multiple cell types.

Characterization of Antiviral Hits and Identification of Compounds that Exacerbate Viral Infection. To stratify compounds, we performed a time-of-addition study with compound added either 4 h prior to infection (as done previously in the screen) or 1 h p.i. (Fig. 4*A*). We infected Huh7 with SARS-CoV-2 at MOI of 1 and

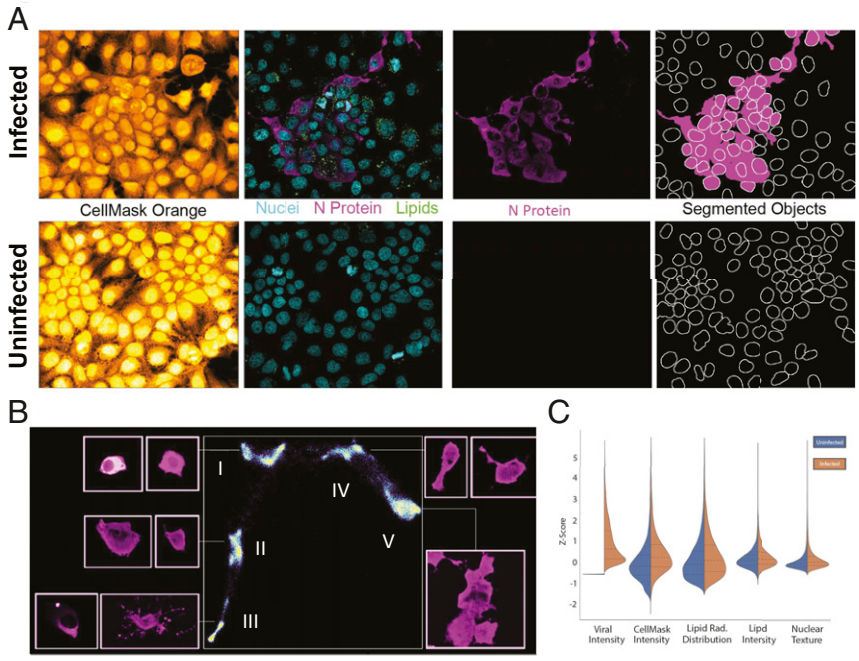

Fig. 1. Morphological profiling of SARS-CoV-2–infected Huh7 cells (MOI of 0.2 for 48 h). (*A*) Clockwise: Representative field with nuclei (cyan), neutral lipids (green), and SARS-CoV-2 N protein (magenta), N-protein image in the same area with "fire" false color LUT showing distinct morphologies of infected cells showing small/round cells with a hollow center, cells with protrusions, and large syncytia, CellMask image showing cell boundaries and syncytia formation. (*B*) UMAP embedding and phenotypic clustering of 3 million cells exhibiting viral stain show distinct morphologies, including small/bright cells (I), cells with protrusions (III), and syncytia (V). (*C*) Comparison of normalized cellular features in infected (brown) and uninfected (blue) cells showing differences in cytoplasmic organization, lipid content/distribution, and nuclear texture. All distributions were compared with the Mann–Whitney test and are statistically significant with $P < 0.0001$.

then quantified infection by detecting the positive-strand viral RNA genome by RNAscope (Fig. 4*B*). We found that verapamil, entecavir, and niclosamide lost activity under these experimental conditions (Fig. 4*C*). Amiodarone, clofazimine, S1RA, lomitapide, Z-FA-FMK, the other nucleoside analogs remdesivir and thioguanine, and the kinase inhibitors bosutinib, fedratinib, and gilteritinib retained activity regardless of compound addition preinfection or postinfection, suggesting that they inhibit postbinding events. Two compounds, ipratropium bromide and metoclopramide, lost activity when added 1 h p.i., suggesting a role in viral binding inhibition. Although they share the same molecular target (dopamine D2 receptor), metoclopramide and domperidone seem to exert their antiviral activity with different modes of action, either by directly inhibiting binding or indirect effects on the host. Cell counts are shown in *SI Appendix*, Fig. S3 for drug treatments in Fig. 4 and demonstrate the lack of cytotoxicity.

Our screening also identified compounds that exacerbated infection. All mitogen/extracellular signal-regulated kinase (MEK) inhibitors tested (cobimetinib, trametinib, and binimetinib) resulted in a greater than twofold increase of viral infection in Huh7 (Fig. 5 *A* and *B*). To confirm this finding, we performed RNAscope on virus-infected, cobimetinib-treated versus untreated cells 24 and 48 h p.i. (Fig. 5*C*). The percentage of viral RNA-positive cells was increased at 48 h p.i., but not at 24 h p.i., following treatment, suggesting that these compounds could enhance virus spread. In addition, upon treatment with the three MEK inhibitors, and cobimetinib in particular, we observed an increased syncytia size (Fig. 5*A*) and more diffuse viral RNA and S protein staining pattern within the infected cells (Fig. 5*D*). These immunofluorescence staining patterns suggest a difference in viral compartmentalization and spread in MEK inhibitor-treated cells. The increased infection and the diffuse localization of viral RNA was recapitulated when treating the cells with a molecular probe, U0126 (10 μM), that is commonly used as an inhibitor of the Ras–Raf–MEK–ERK pathway (Fig. 5*E*). Mek inhibitors were also evaluated in Caco-2 cells, where the exacerbation effect was observed for trametinib and binimetinib, albeit at a higher concentration of 10 μM (*SI Appendix*, Fig. S4). Cell counts are shown in *SI Appendix*, Fig. S3 for drug treatments in Fig. 5 and indicate the lack of cytotoxicity at the tested doses. Taken together, these data highlight the utility of screening FDA-approved compounds as a way of identifying cellular pathways involved in viral infection.

Lactoferrin Blocks SARS-CoV-2 Replication at the Entry Level. The most broadly efficacious hit identified was lactoferrin, a protein found in colostrum and airway epithelium (18). To confirm our previous finding of inhibition of N-protein expression by lactoferrin, we infected Huh7 cells with SARS-CoV-2 (MOI of 0.2) under increasing doses of bovine lactoferrin and measured viral RNA using RT-qPCR at 48 h p.i. (Fig. 6*A*). Lactoferrin exhibited a dose-dependent inhibition of viral replication (Fig. 6*A*) and retained antiviral activity through a range of MOIs (Fig. 6*B*). It maintained antiviral activity even when added 1 or 24 h after infection, suggesting multiple modes of antiviral action (Fig. 6*B*). To rule out iron chelation as a potential mode of action, iron-saturated hololactoferrin and transferrin were tested in Huh7 cells; the former retained activity and the latter was inactive (Fig. 6*C*). Given the pronounced single-agent efficacy of lactoferrin, we further tested whether combinations with the FDA-approved agent remdesivir could improve the overall antiviral activity. To test for synergy between lactoferrin and remdesivir treatments, we measured the percent infection over 8 × 8 dose combinations, in two technical and two biological replicates along with single agents, DMSO vehicle, and mock infection controls. The negative control (DMSO vehicle) infection rate for the two plates were 21.6% with the 95% credible interval (CI95) of [20.8, 22.5] and 11.6% with CI95 = [11, 12.2], respectively, with no significant loss of cell viability/reduction in cell counts (*SI Appendix*, Fig. S3*C*). The maximum efficacy for each treatment and the combination were similar and not significantly different from the no-viral control of 0.004% infected cells remaining. We found the IC_{50} for remdesivir to be 6.7 nM with CI95 of [6.1, 7.5] and 440 nM with CI95 of [360, 520] for lactoferrin, consistent with previous experiments. To model the synergy, we fit the Bayesian MuSyC model (19) and found the synergistic potency parameter alpha to be 1.5 with CI95 = [0.6, 3.7], indicating that lactoferrin and remdesivir are not significantly synergistic or antagonistic but do exhibit additive efficacy. To visualize, we normalized the infection rate for each plate by the estimated top infection rate and plotted the median for each dose combination, with level sets of the MuSyC fit as shown in Fig. 6*E*. None of the treatments shown

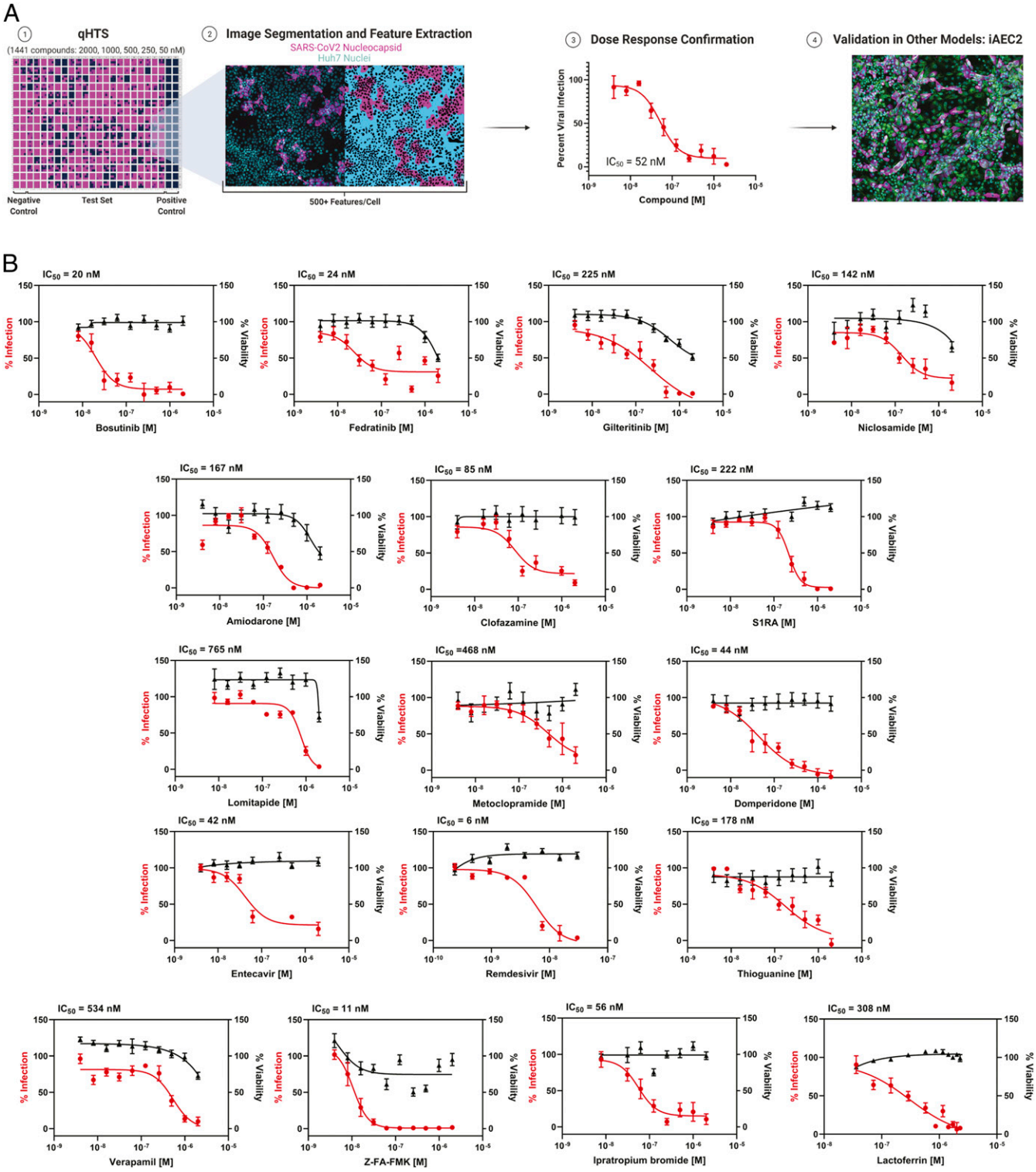

Fig. 2. Screen to identify drugs with antiviral activity against SARS-CoV-2. (*A*) Schematic of the anti–SARS-CoV-2 drug repurposing screening. 1) Compounds are administered in qHTS to cells cultured on 384-well plates infected with SARS-CoV-2 and incubated for 48 h. Each plate contains 32 negative (infected) and 32 positive (noninfected) control wells. 2) Cells are fixed, stained, and imaged. Images are analyzed using Cell Profiler to identify nuclei, cell boundaries, neutral lipid content, and viral staining intensity. 3) Dose–response curves are fit to normalized percent infected cells per well. 4) Confirmation of antiviral activity in other cell lines, including a physiologically relevant iPSC-derived human alveolar epithelial cell (iAECs); (*B*) Dose–response curves of 17 compounds. Graphs represent median SEM of 10-point 1:2 dilution series of selected compounds for $n = 3$ biological replicates. IC_{50} values were calculated based on normalization to the control and after fitting in GraphPad Prism.

Table 1. Compound summary

ID, Drug Bank ID	Compound name	Indication	General mechanism of action	Potential mode of action against SARS-CoV2	IC_{50}, nM; Huh-7	IC_{90}, nM; Huh-7	IC_{50}, nM; Vero E6	IC_{50}, nM; Caco-2	IC_{50}, nM; LNcaP	IC_{50}, nM; iAEC2	Serum CMax, nM	Route of administration	CMax:IC90 Huh7	Ref.
DB01118	Amiodarone (hydrochloride)	Treatment of ventricular tachycardia	Inhibitor of K and Ca channels	Entry inhibitor, evaluated in clinical trial for COVID19 (NCT04351763)	**167**	404	**1,406**	**5,500**	**>5,000**	**118**	4,960	Oral (800 mg)	12.28	50
DB06616	Bosutinib	Treatment of chronic myeloid leukemia	Bcr-Abl kinase inhibitor	Inhibitor of S protein fusion similar to the related Imatinib	20	80	>5,000	IA	Inverse	IA	310	Oral (500 mg)	3.88	51
DB00845	Clofazimine	Treatment of leprosy	Binds to mycobacterial DNA and K transporters inhibitor	Entry inhibitor, evaluated in clinical trial for COVID19 (NCT04465695)	85	>2,000	>5,000	>5,000	29	>5,000	866	Oral (200 mg)	<0.43	61
DB01184	Domperidone	Antiemetic	Dopamine D2 receptor antagonist	Host modulation	44	233	IA	IA	ND	IA	44	Oral (20 mg)	0.19	53
DB00442	Entecavir (hydrate)	Treatment of hepatitis B virus	Transcription inhibitor, nucleoside analog	Replication inhibitor	42	>2,000	>5,000	IA	IA	IA	15	Oral (1 mg)	<0.0075	54
DB12500	Fedratinib	Treatment of intermediate-2 and high-risk primary and secondary myelofibrosis	Tyrosine kinase inhibitor (Jak1)	Predicted inhibitor of kinase (NAK) family reported to reduce viral infection in vitro. Reduction of TH17 responses responsible of SARS-CoV-2 associated cytokine storm	24	>2,000	>5,000	>5,000	>5,000	1,810	3,483	Oral (400 mg)	<1.74	55
DB12141	Gilteritinib	Treatment of FLT3-mutated acute myeloid leukemia (AML)	FMS-like tyrosine kinase 3 (FLT3) inhibitor	Host modulation	225	722	2,344	IA	IA	>5,000	677	Oral (120 mg)	0.94	56
DB00332	Ipratropium Bromide	Treatment of COPD and asthma	Muscarinic receptor antagonist	Binding inhibitor	**56**	>2,000	**NA**	**85**	**>5,000**	**4**	NA	Aerosol/nasal spray	NA	NA
NA	Lactoferrin	Dietary supplement	Iron chelator, immune-modulator, antimicrobial activity	Entry and post-entry inhibitor	**308**	4,108	**NA**	**1,170**	**157**	**45**	NA	Oral (250 mg)	NA	NA
DB08827	Lomitapide	Treatment of homozygous familial hypercholesterolemia	Microsomal triglyceride transfer protein (MTP) inhibitor	Host lipid metabolism modulation	**765**	1,440	**1,875**	**>5,000**	**IA**	**733**	1.7	Oral (60 mg)	0.0012	57
DB01233	Metoclopramide	Treatment of diabetic gastroparesis	Dopamine D2 and serotonin 5-HT3 receptor inhibitor	Binding inhibitor	468	>2,000	>5,000	IA	IA	IA	147	Oral (20 mg)	<0.0734	58
DB06803	Niclosamide	Treatment of tapeworm infections	Mitochondrial uncoupler, mTORC1 inhibitor	Autophagy and endocytic pathway inhibitor	142	>2,000	>5,000	IA	>5,000	NA	18,300	Oral (2 g)	<9.15	59
DB14761	Remdesivir	Investigational for Ebola virus treatment	Transcription inhibitor, nucleoside analog	Replication inhibitor, emergency FDA approval for COVID19	6	15	NA	19	106	18	3,700	Intravenous	246.67	60
ZINC95000617	S1RA	Treatment of neuropathic pain (phase II)	Sigma R1/R2 modulator	Entry inhibitor	222	456	>5,000	>5,000	IA	1	11,670	Oral (500 mg)	25.59	61
DB00352	Thioguanine	Therapy of acute leukemia	Guanine analog	Replication inhibitor	178	1,854	820	674	29	IA	311	Oral (40 mg)	0.17	62
DB00661	Verapamil (hydrochloride)	Treatment of high blood pressure, heart arrhythmias, and angina	Ca channel inhibitor	Entry inhibitor Evaluated in clinical trial for COVID19 (NCT04351763)	534	1,444	>5,000	Low	18	NA	880	Oral (240 mg)	0.61	63
CAS 197855–65-5	Z-FA-FMK	Preclinical	Irreversible inhibitor of cysteine proteases (cathepsin L)	Entry inhibitor	**11**	28	**51**	**Low**	**514**	**4**	NA	NA	NA	NA

NA, not tested; IA, inactive; >5,000 indicates activity but loss of potency; low, IC_{50} below 1 nM. Gray rows with bold text indicate compounds with efficacy across multiple cell systems.

in Fig. 6 exhibited any loss of cell viability/reduction in cell counts (*SI Appendix*, Fig. S3*C*).

Previous work on lactoferrin in the context of SARS-CoV-1 suggested that lactoferrin blocks viral entry by binding heparan sulfate proteoglycans, which are viral attachment factors. Heparan sulfates are also SARS-CoV-2 attachment factors (20). Therefore, we performed a viral binding assay by incubating SARS-CoV-2 (MOI of 10) in the presence of lactoferrin (1,250 and 6,250 nM) for 1 h on ice followed by quantification of viral RNA by RT-qPCR (Fig. 6*D*). Remdesivir was included as a negative control as it blocks viral infection at a postbinding step. Both concentrations of lactoferrin, but not remdesivir, blocked SARS-CoV-2 attachment to Huh7 cells (Fig. 6*D*). As a positive control, Huh7 cells were treated with $NaClO_3$, a protein sulfation inhibitor that depletes cells of heparan sulfate (21). SARS-CoV-2 binding to cells was reduced in $NaClO_3$-treated cells, and additional lactoferrin treatment did not further reduce binding (Fig. 6*D*). These data suggest that similar to SARS-CoV-1, lactoferrin blocks viral attachment via neutralizing heparan sulfate proteoglycans.

Lactoferrin Elicits Inflammatory Responses that May Suppress Infection by SARS-CoV-2. Another potential mechanism of action of lactoferrin is through enhancement of inflammatory responses, which can then limit viral replication within host cells (22). We evaluated mRNA levels of IFNβ and the interferon-stimulated genes ISG15, MX1, Viperin, and IFITM3 in lactoferrin-treated infected Huh7 cells (*SI Appendix*, Fig. S2). SARS-CoV-2 infection did not result in a robust interferon response consistent with previous studies (23). However, we did detect an up-regulation of IFNβ and interferon-stimulated gene transcripts in virus-infected and lactoferrin-treated cells, suggesting that the post-entry antiviral activity of lactoferrin may be interferon-mediated. Since Huh7 cells have defects in innate immune signaling (24), we used the more physiologically relevant model of the iAEC2 cells to detect transcriptomic changes of uninfected cells upon treatment with lactoferrin at the efficacious concentration of 6.25 μM. Our data showed significant changes in the transcription of genes after 48 h of lactoferrin treatment with 1,016 and 1,023 genes significantly up- and down-regulated, respectively (Fig. 7*A*). Interestingly, one of the top up-regulated genes was the secretoglobin 3A2 (SCGB3A2). It is the only secretoglobin expressed in this alveolar lineage (other secretoglobins being mostly marker of airways cells), and it has been widely reported as an anti-inflammatory protein in the context of allergic reaction to house dust mites (25). Pathway analysis revealed an induction of the anti-inflammatory TNFα pathway via NFκB (Fig. 7*B*) with specific up-regulation of transcripts for interferon-stimulated genes: *TRIM25*, *ISG20*, *IFIT2*, but also for interferon receptor α and γ (*IFNAR1* and *IFNARG2*, respectively) (Fig. 7*C*). Notably, an up-regulation of *IRF9* and *STAT2* was also observed, consistent with the activation of a noncanonical antiviral and immunoregulatory program triggered by the combination of IFNβ and TNFα (26) (Fig. 7*C*). Altogether, these data suggest that lactoferrin likely exerts both direct and indirect antiviral action by inhibiting entry and by inducing an antiviral program that may suppress SARS-CoV-2 replication by host cell machinery.

Discussion

In this study, we developed an experimental workflow based on high-content imaging and morphological profiling that allows for rapid screening of FDA-approved compounds and identified 17 compounds that inhibit SARS-CoV-2 infection in vitro. Of these, seven were previously reported and serve as a benchmark validation of our endpoints and experimental approach, and 10 were hitherto unknown. We evaluated the antiviral activity of the 17 hits identified in Huh7 in three transformed cell lines (VeroE6, Caco-2, and LNcaP) and one nontransformed cell line (iAECs) and observed six compounds (amiodarone, ipratropium bromide, lactoferrin, lomitapide, remdesivir, Z-FA-FMK) exhibiting activity across multiple cell lines.

Since the completion of this screen (June 2020), over 30 studies reporting SARS-CoV-2 antiviral activity of FDA-approved drugs have been published. A meta-analysis of these in vitro screens (including this effort) show consensus around 11 compounds, with small total overlap between studies (27). This observation suggests that drug screening of FDA-approved compounds is highly dependent on the chosen cell line and infection conditions. It is expected that compounds exerting an antiviral effect through direct binding to viral proteins would be more independent of the chosen cell system rather than drugs modulating host cell factors that can vary widely by cell type. For example, we observed conserved activity across cell systems for remdesivir, which directly inhibits the viral polymerase (28); lomitapide, which is proposed to directly inhibit SARS-CoV-2 main protease (Mpro) (29); and lactoferrin, which we have shown directly inhibits viral entry.

As most FDA-approved drugs are optimized against human molecular targets, active compounds can lead to target identification of host factors involved in SARS-CoV-2 infection. Z-FA-FMK is an irreversible cathepsin L inhibitor that exhibits potent antiviral activity in all of the five cell systems tested herein because cathepsin L has been shown to be an entry factor of SARS-CoV-2 through the late endolysosome (30, 31). Another hit in our Huh7 screen, fedratinib, was approved by the FDA in 2019 for myeloproliferative neoplasms (32) and is an orally bioavailable semi-selective JAK1/JAK2 inhibitor. JAK inhibitors have been proposed for COVID-19 treatment to specifically inhibit the Th17-mediated inflammatory response (33, 34) and to block numb-associated kinase responsible for clathrin-mediated viral endocytosis (35). The JAK inhibitor baricitinib (36) in combination with remdesivir was granted emergency use authorization by the FDA in late 2020, while jakotinib (ChiCTR2000030170) and ruxolitinib (ChiCTR2000029580) are currently being evaluated in clinical trials for COVID-19 as potential dual action therapeutics (antiviral and innate immune response inhibitors).

In contrast to the antiviral drug hits, we report the connection between MEK inhibition and exacerbated SARS-CoV-2 infection, likely by increasing cell-to-cell spread as suggested by the formation of larger syncytia and more diffuse localization of viral RNA and S protein within infected cells (Fig. 5). Intriguingly, in the context of other virus infections, including SARS-CoV-1, pharmacological inhibition of the Ras–Raf–MEK–ERK pathway results in restriction of viral infection (37). This underscores the importance of this pathway during viral infections and warrants further examination into the mechanism of action of this signaling cascade during SARS-CoV-2 infection.

This study has generated several clinically testable and readily translatable hypotheses. As an example, we observed potent antiviral activity of ipratropium bromide (Atrovent), a quaternary ammonium salt and muscarinic receptor antagonist that is commonly prescribed for asthma. It is administered via inhalation into the lungs with little systemic absorption. Given its potential mode of action as inhibitor of SARS-CoV-2 attachment, prophylaxis or postexposure treatment with ipratropium bromide may curb infection of the upper respiratory tract and drastically reduce systemic viral spread and development of severe symptoms while achieving beneficial bronchodilation. Similarly, we identified metoclopramide and domperidone, both dopamine D2 receptor antagonists used to treat gastrointestinal symptoms, as SARS-CoV-2 inhibitors. Gastrointestinal symptoms have been increasingly reported in more than half of the patients infected by SARS-CoV-2 (2). Hence, these compounds may ameliorate gastrointestinal (GI) symptoms during COVID-19 infection, and, in addition, the reduced viral load in the GI tract could also reduce fecal-oral transmission of SARS-CoV-2 (38). Consistent with our findings, the approved leprosy drug clofazamine was recently shown to not only have antiviral activity in cells, but block

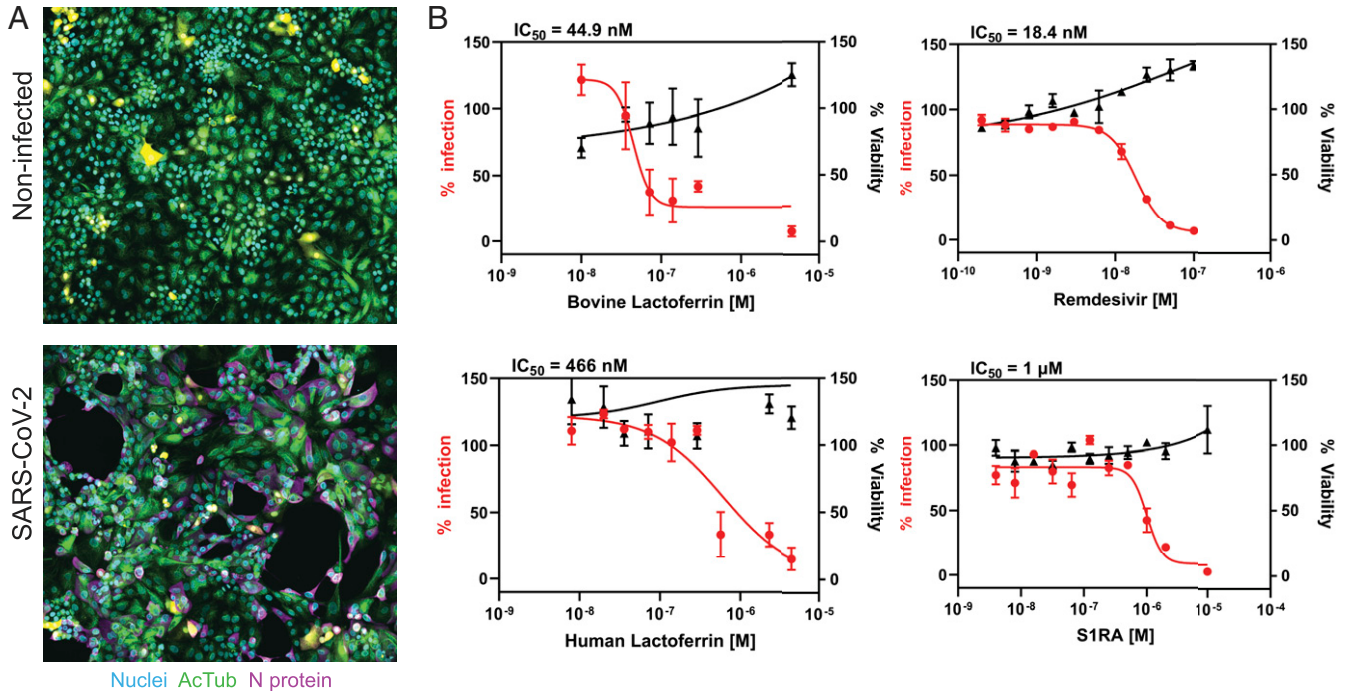

Fig. 3. Validation of candidate compounds in iAEC2 cells infected with SARS-CoV-2. (*A*) SARS-CoV-2–infected iAEC2 cells at MOI of 10, 48 h post infection (p.i.). Nuclei are in cyan, N protein in magenta, and acetylated tubulin in green. Representative image was acquired on a Yokogawa CQ1 high-content imager with a 60× lens and visualized with Fiji ImageJ. Cellular protrusions are indicated with white arrows. (*B*) Antiviral activity of bovine and human lactoferrin, remdesivir, and S1RA was assessed in iAEC2 cells infected with SARS-CoV-2 at MOI 10. Graphs represent median SEM of 10-point 1:2 dilution series of selected compounds for $n = 3$ biological replicates.

viral infection in a hamster model of disease (39), making it a strong candidate for clinical translation.

Most noteworthy, our screen identified bovine lactoferrin, a safe and widely available dietary supplement, with multimodal efficacy in multiple cell systems, including nontransformed and physiologically relevant iAEC2s. Our study is the only repurposing discovery effort that included several proteins (like lactoferrin), as conventional high-throughput screening is generally limited to small molecules in DMSO. Lactoferrin gene expression was shown to be highly upregulated in response to SARS-CoV-1 infection (40), and in addition to enhancing natural killer cell and neutrophil activity, lactoferrin blocks SARS-CoV-1 attachment through binding to heparan sulfate proteoglycans (20). Here, we showed that lactoferrin likely has a multimodal mechanism of action against SARS-CoV-2 infection (Figs. 6 and 7). First, it strongly inhibited cellular binding of SARS-CoV-2 to cells via competition with heparan sulfate. Second, it modulated host cell innate immune responses through increased expression of interferon-stimulated genes and TNFα. Through heightening the innate immune response of host cells, orally administered lactoferrin could be effective in resolving the GI symptoms that are present in COVID-19 patients (41) with a mechanism similar to norovirus infection (42). In addition, lactoferrin was previously shown to decrease the production of IL-6 (43), which is one of the key players of the "cytokine storm" produced by SARS-CoV-2 infection (44, 45). Bovine lactoferrin, widely available as 250-mg gelatin capsules for oral administration, is classified by the FDA as "generally recognized as safe" and therefore may represent a promising therapy for preexposure and postexposure prophylaxis. As a therapeutic intervention for COVID-19, lactoferrin might exert direct antiviral and anti-inflammatory efficacy in the airway with alternative routes of administration like intranasal delivery or in a nebulized formulation delivered to the lungs.

Combination therapies are likely to be required for effectively treating SARS-CoV-2 infection, and this approach has already shown promise, i.e., combination therapy with interferon β-1b, lopinavir–ritonavir, and ribavirin showed efficacy against SARS-CoV-2 in a prospective, open-label, randomized, phase 2 trial (46). Here, we show that lactoferrin potentiates the antiviral activity of remdesivir and could be used in combination therapy with these drugs, which are currently being used or studied for the treatment of COVID-19. Due to its wide availability, limited cost, and strong safety profile, lactoferrin could be a rapidly deployable option for both prophylaxis and the management of COVID-19. Although our findings are promising and have led to several clinical studies, further studies are needed to confirm the efficacy of our lead antiviral compounds in animal models and/or clinical studies.

Methods

Cells and Virus. Vero E6, Caco-2, LNCaP, and Huh7 cells were maintained at 37 °C with 5% CO_2 in Dulbecco's modified Eagle's medium (DMEM) (Wellgene), supplemented with 10% heat-inactivated fetal bovine serum (FBS), Hepes, nonessential amino acids, L-glutamine, and 1× antibiotic-antimycotic solution (Gibco). iPSC (SPC2 iPSC line, clone SPC2-ST-B2, Boston University) derived alveolar epithelial type 2 cells (iAEC2s) were differentiated and maintained as alveolospheres embedded in three-dimensional (3D) Matrigel in "CK+DCI" media, as previously described (47). iAEC2s were passaged approximately every 2 wk by dissociation into single cells via the sequential application of dispase (2 mg/mL; Thermo Fisher Scientific; 17105-04) and 0.05% trypsin (Invitrogen; 25300054) and replated at a density of 400 cells/μL of Matrigel (Corning; 356231), as previously described (40). SARS-CoV-2 was deposited by the Centers for Disease Control and Prevention and obtained through BEI Resources, National Institute of Allergy and Infectious Diseases, NIH: SARS-Related Coronavirus 2, Isolate USA-WA1/2020, NR-52281. Lack of genetic drift of our viral stock was confirmed by deep sequencing. Viral titers were determined by TCID50 assays in Vero E6 cells (Reed and Muench method) by microscopic scoring. All experiments using SARS-CoV-2 were performed at the University of Michigan under Biosafety Level 3 (BSL3) protocols in compliance with containment procedures in laboratories

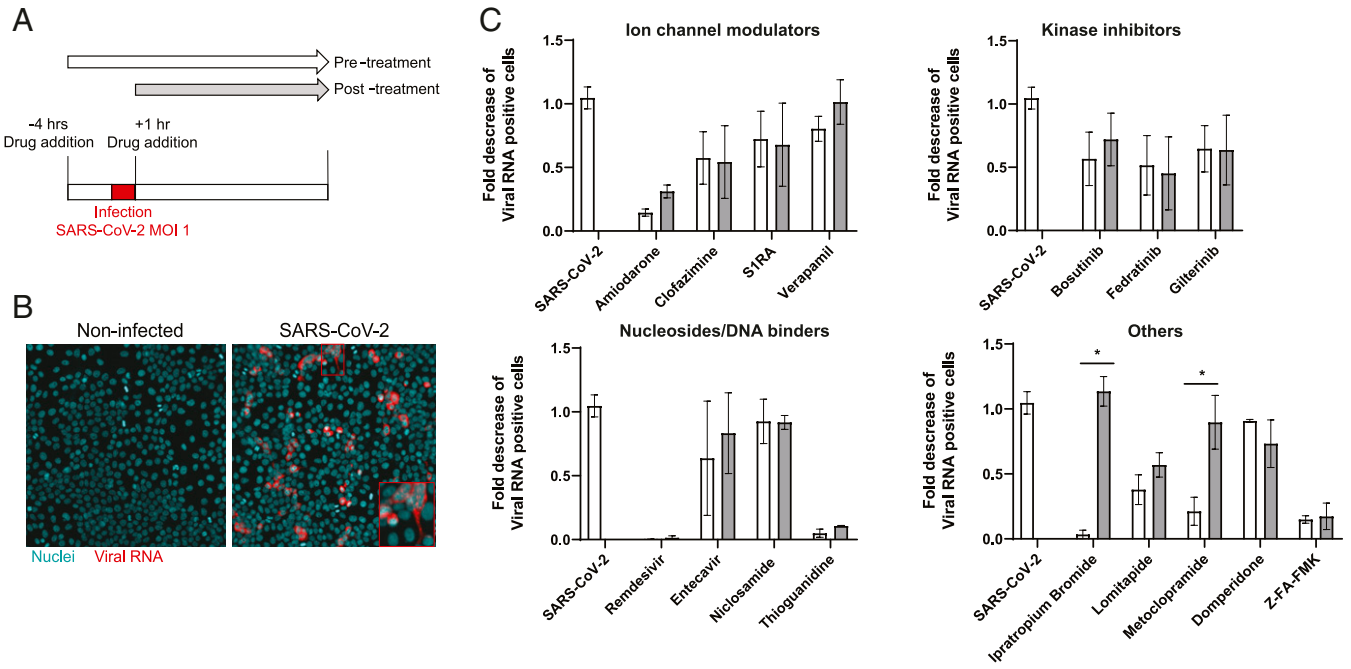

Fig. 4. Time-of-addition study with the identified antiviral hits. (*A*) Experimental scheme where compounds are added 4 h prior (same treatment window as drug screening) or 1 h post infection (p.i.) with SARS-CoV-2 (MOI of 1). Huh7 cells are fixed, permeabilized, and subjected to RNAscope analysis 48 h p.i. (*B*) Representative image of SARS-CoV-2–infected and noninfected Huh7 cells acquired on the CX5 high-content platform at 10× and analyzed with Fiji ImageJ. Viral RNA is represented in red, and nuclei in cyan. (*C*) Time of drug-addition for selected antiviral hits (at 10× IC_{50} dose) organized according to the compound class. Graphs represent the fold decrease of infection over the untreated condition. Infection was calculated on the viral RNA image after image segmentation with Cell Profiler. Graphs represent an average SEM of $n = 3$ biological replicates. Statistical significance determined using multiple Student's *t* test with the Bonferroni–Dunn correction method, with $\alpha = 0.05$. $^*P < 0.01$.

approved for use by the University of Michigan Institutional Biosafety Committee and Environment, Health and Safety.

Viral Infectivity Assay. The 384-well plates (Perkin-Elmer, 6057300) were seeded with Huh7 cells at 3,000 cells/well and allowed to adhere overnight. Compounds were then added to the cells and incubated for 4 h. The plates were then transferred to BSL3 containment and infected with SARS-CoV-2 WA1 at a MOI of 0.2 in a 10-μL addition with shaking to distribute virus. For the final dose–responses curves, porcine trypsin (Sigma-Aldrich; T0303) at a final concentration of 2 μg/mL was included during infection. After 1 h of absorption, the virus inoculum was removed and fresh media with compound was added. Uninfected cells and vehicle-treated cells were included as positive and negative control, respectively. Two days postinfection, cells were fixed with 4% paraformaldehyde (PFA) for 30 min at room temperature, permeabilized with 0.3% Triton X-100, and blocked with antibody buffer (1.5% BSA, 1% goat serum, and 0.0025% Tween 20). The plates were then sealed, surface decontaminated, and transferred to BSL2 for staining with the optimized fluorescent dye-set: anti-nucleocapsid protein (anti-NP) SARS-CoV-2 antibody (Antibodies Online; catalog no. ABIN6952432) overnight treatment at 4 °C followed by staining with secondary antibody Alexa-647 (goat anti-mouse; Thermo Fisher; A21235), Hoechst-33342 pentahydrate (bis-benzimide) for nuclei staining (Thermo Fisher; H1398), HCS LipidTOX Green Neutral Lipid Stain (Thermo Fisher; H34475), and HCS CellMask Orange for cell delineation (Thermo Fisher; H32713). iAEC2 maintained in 3D culture were dissociated to single cells and seeded in collagen-coated 384-well plates at a seeding density of 8,000 cells/well in the presence of 10 μM Y-27632 for the first 72 h after plating (APExBIO; A3008) to grow to roughly 80% confluence. Infection was performed at MOI of 10 in the presence of 2 μg/mL trypsin porcine (Sigma-Aldrich, T0303). Staining protocol for the iAEC2s differed slightly with the addition of an anti-acetylated tubulin primary antibody (Cell Signaling; 5335), instead of HCS CellMask Orange, and the use of an additional secondary Alexa 488 antibody (donkey anti-rabbit; Jackson ImmunoResearch; 711-545-152).

Compound Library. The compound library deployed for drug screening was created using the FDA-Approved Drugs Screening Library (Item No. 23538) from Cayman Chemical Company. This library of 875 compounds was supplemented with additional FDA-approved drugs and selected clinical candidates from other vendors including MedChemExpress, Sigma-Aldrich, and Tocris. Clinical candidates and chemical probes were included if they had any reported antiviral efficacy or had an association with SARS1, MERS, or SARS-CoV-2. The library was formatted in five 384-well compound plates and was dissolved in DMSO at 10 mM. Apolactoferrin was provided by Glanbia Nutritionals (Bioferrin 2000); Hololactoferrin (Sigma-Aldrich; L4765), native human lactoferrin (Creative BioMart; LFT-8196H), and transferrin (Sigma-Aldrich; T2036) were handled separately and added manually in cell culture media. Dilution plates were generated for qHTS at concentrations of 2 mM, 1 mM, 500 μM, 250 μM, and 50 μM, and compounds were dispensed at 1:1,000 dilution.

qHTS Primary Screen and Dose–Response Confirmation. For the qHTS screen, compounds were added to cells using a 50-nL pin tool array on a Caliper Life Sciences Sciclone ALH 3000 Advanced Liquid Handling system. Concentrations of 2 μM, 1 μM, 500 nM, 250 nM, and 50 nM were included for the primary screen. In all dose–response confirmation experiments, compounds were dispensed using an HP D300e Digital Compound Dispenser and normalized to a final DMSO concentration of 0.1% DMSO. Dose–response confirmation was performed in triplicate and in 10-point/twofold dilution. Z-primes for dose–response plates ranged between 0.4 and 0.8.

Imaging. Stained cell plates were imaged on both Yokogawa CQ1 and Thermo Fisher CX5 high-content microscopes with a 20×/0.45 N.A. LUCPlan FLN objective. Yokogawa CQ1 imaging was performed with four excitation laser lines (405 nm/488 nm/561 nm/640 nm) with spinning disk confocal and 100-ms exposure times. Laser power was adjusted to yield optimal signal-to-noise ratio for each channel. Maximum intensity projection images were collected from five confocal planes with a 3-μm step size. Laser autofocus was performed and nine fields per well were imaged covering ∼80% of the well area. The Thermo Fisher CX5 with LED excitation (386/23 nm, 485/20 nm, 560/25 nm, 650/13 nm) was also used and exposure times were optimized to maximize signal/background. Nine fields were collected at a single *Z*-plane as determined by image-based autofocus on the Hoechst channel. The primary qHTS screen was performed using CX5 images, and all dose–response plates were imaged using the CQ1.

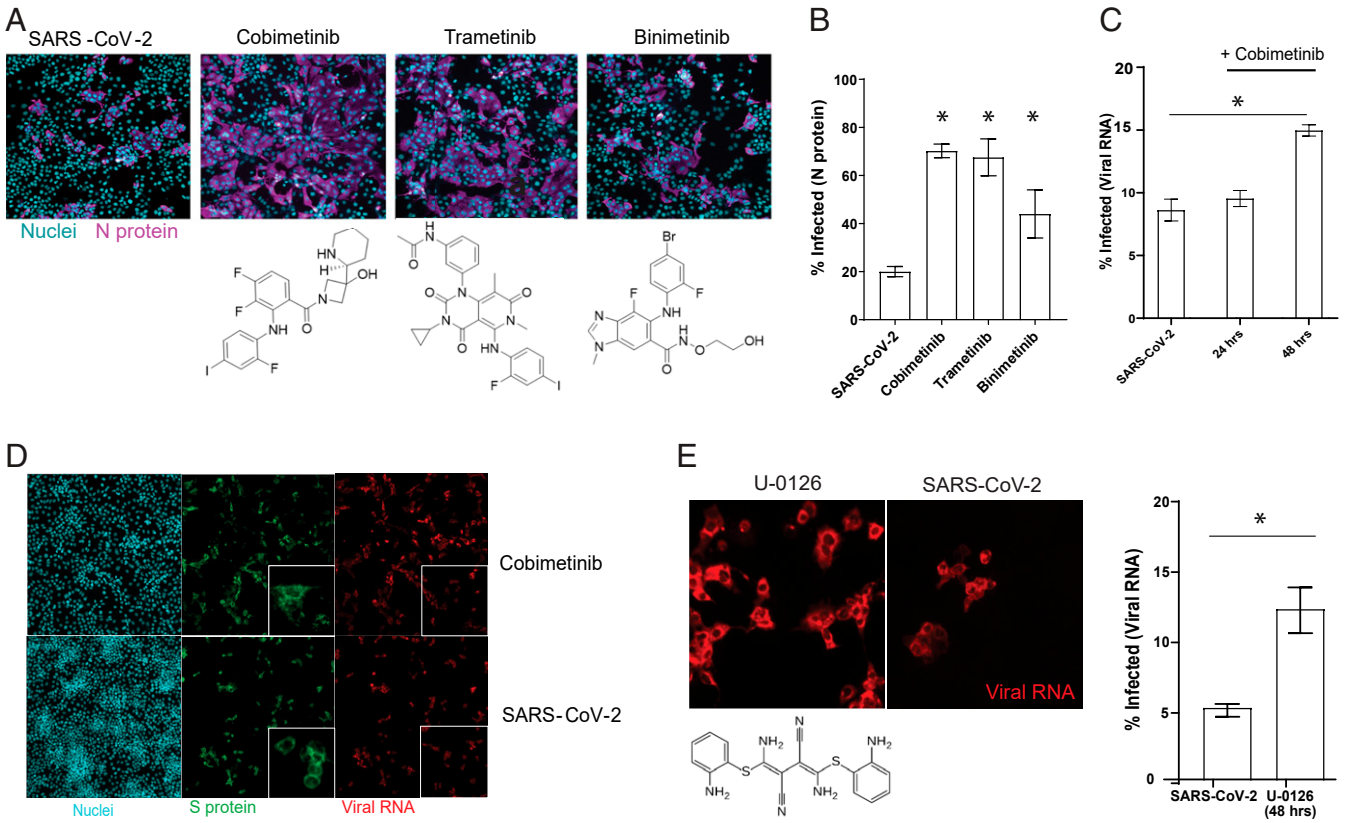

Fig. 5. Selective MEK inhibitors exacerbate SARS-CoV-2 infection. (*A*) Representative images of Huh7 cells infected with SARS-CoV-2 (MOI of 0.2) and treated with cobimetinib (250 nM), trametinib (250 nM), and binimetinib (250 nM) with nuclei in cyan and N protein in magenta. Viral infection was calculated on N-protein images after image segmentation with Cell Profiler. Bars represent $n = 3$ technical replicates and unpaired t tests with Welch's correction were performed in GraphPad Prism. *$P < 0.001$. (*B*) Quantitation of percent infection with MEK inhibitors. (*C*) RNAscope of Huh7 infected with SARS-CoV-2 (MOI of 1) treated with cobimetinib (1,000 nM) and harvested at 24 and 48 h p.i. Graph represents average, SEM of $n = 3$ biological replicates. (*D*) Representative images of SARS-CoV-2–infected (MOI of 1) and cobimetinib (1,000 nM)-treated Huh7. Cells were harvested 48 h p.i., subjected to RNAscope to detect viral RNA (positive strand, in red) and counterstained with anti-S protein antibody (green) and Hoechst 33342 (nuclei in cyan). (*E*) SARS-CoV-2–infected (MOI of 1) Huh7 were treated with U-0126 (10 μM) and subjected to RNAscope 48 h p.i. Graph represents average SEM of $n = 2$ biological replicates, each with three technical replicates. Corresponding viability data for compound treatments is shown in *SI Appendix*, Fig. S3*A*.

Image Segmentation, Feature Extraction, and Infection Score. The open source CellProfiler software (10) was used in an Ubuntu Linux-based distributed Amazon AWS cloud implementation for segmentation, feature extraction, and infection scoring, and results were written to an Amazon RDS relational database using MySQL. A pipeline was developed to automatically identify infected cells in a field and to enable cell-level morphologic profiling. Infected areas were identified by Otsu thresholding and segmentation using the N-protein image, then all nuclei were identified in a similar manner in the Hoechst-33342 image, and the "relate objects" module was used to relate nuclei to an infected cell area. If a nucleus was found to reside within an infected area, then it and its corresponding cell area was labeled "infected." The percentage of infected cells was tabulated by dividing the infected cell number by the total cell number summed across nine fields per well. To enable morphologic cell profiling, the following ROIs were defined for feature extraction: nuclei, cell, cytoplasm, nucleoli, neutral lipid droplets, and syncytia. Multiple intensity features and radial distributions were measured for each object in each channel, and cell size and shape features were measured. Nuclei were segmented using the Hoechst-33342 image, and the whole cell mask was generated by expanding the nuclear mask to the edge of the Cell Mask Orange image. Plate-based normalization was performed to account for variability in infection percentage. The assay window was normalized between the positive control wells (32 uninfected wells representing 0% inhibition) and the negative control wells (32 infected wells, 0.1% DMSO vehicle treated representing 100% effect).

Data Preprocessing. Cell-level data were preprocessed and analyzed in the open source Knime analytics platform (48). Cell-level data were imported into Knime from MySQL, drug treatment metadata was joined, and features were centered and scaled. Features were pruned for low variance (<5%) and high correlation (>95%) and resulted in 660 features per cell.

Statistical Methods and Hypothesis Testing. Dose–response curves were fit and pairwise differences between experimental conditions were tested using Prism (GraphPad Software). Other statistical tests, including nonparametric Mann–Whitney, were performed in the statistical programming language and environment R.

UMAP Embedding. The embed_umap application of MPLearn (v0.1.0; https://github.com/momeara/MPLearn) was used to generate UMAP embeddings. Briefly, for a set of cells, each feature was per-plate standardized and jointly orthogonalized using sklearn.IncrementalPCA(n_components = 379, batch_size = 1,000). Then, features were embedded into two dimensions using umap-learn (v0.4.1) (42). UMAP(n_components = 2, n_neighbors = 15, min_dist = 0, init='spectral', low_memory = True). Embeddings were visualized using Holovies Datashader (v1.12.7) (49), using histogram equalization and the viridis color map.

Data Analytics. HC Stratominer (Core Life Analytics) was used as an independent method for hit-calling and performs fully automated/streamlined cell-level data preprocessing and score generation. IC Stratominer was also used to fit dose–response curves for qHTS. Compound registration and assay data registration were performed using the open source ACAS platform (Refactor BioSciences GitHub; https://github.com/RefactorBio/acas).

Dose–Response Analysis and Compound Selection. In qHTS screening, a compound was selected to be carried forward into dose–response confirmation

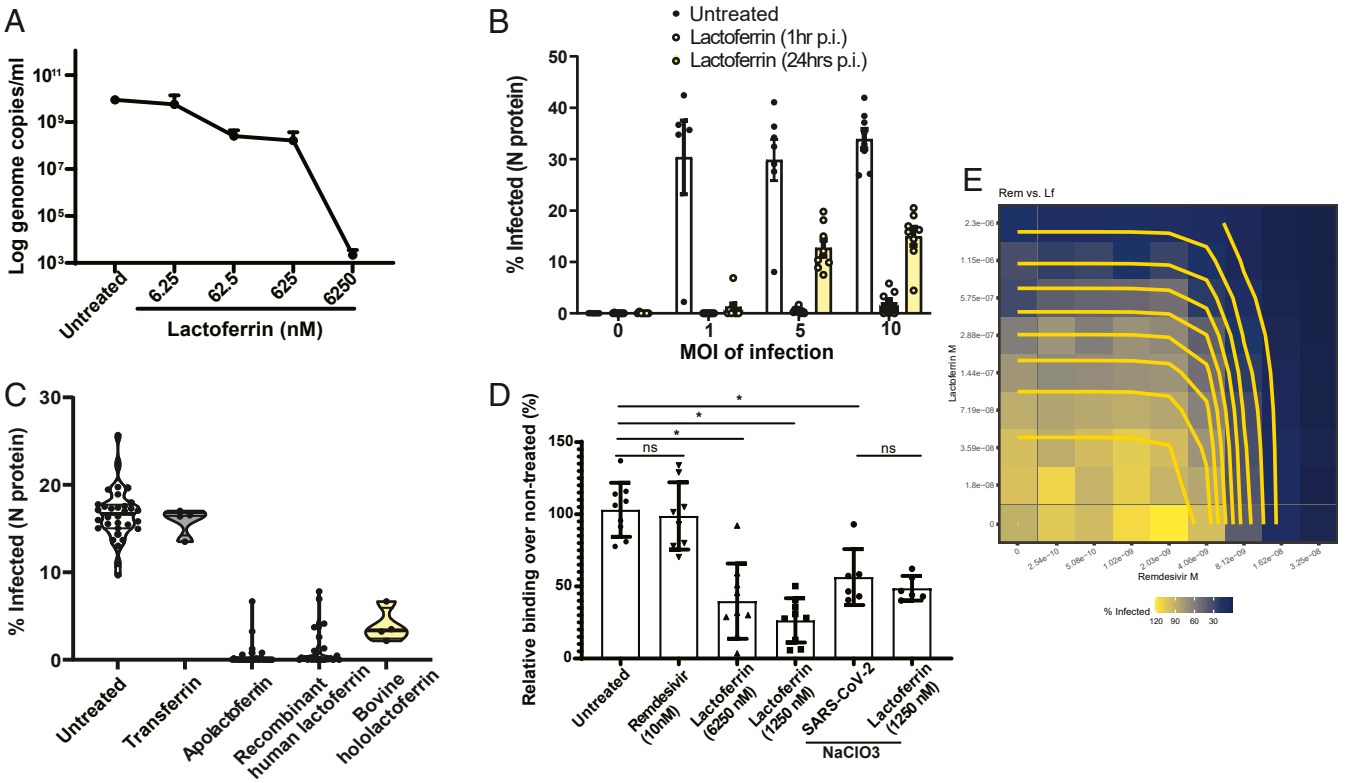

Fig. 6. Lactoferrin blocks SARS-CoV-2 at the attachment step. (*A*) Huh7 cells were infected with SARS-CoV-2 at MOI of 0.2 for 48 h and treated with increasing concentration of lactoferrin (6.25–6,250 nM). Cells were harvested and RNA was extracted. Viral genome copies were calculated by RT-qPCR with an absolute quantification method. (*B*) Huh7 were infected with SARS-CoV-2 (MOI of 1, 5, and 10; MOI of 0 indicates noninfected cells) and treated with 6,250 nM lactoferrin at 1 and 24 h p.i. Bars indicate the percentage of infected cells in different conditions. Data are an average of eight replicates. Statistical significance determined using multiple Student's *t* test with the Bonferroni–Dunn method, with $\alpha = 0.05$. Except for MOI of 0, all conditions (untreated vs. lactoferrin, 1 h or untreated vs. lactoferrin, 24 h) differ by $P < 0.0001$. (*C*) Percentage of SARS-CoV-2–infected Huh7 cells upon treatment with bovine apolactoferrin and hololactoferrin, native human lactoferrin, and transferrin at a concentration of 6,250 nM. (*D*) Binding assay. Huh7 cells were preincubated on ice with compounds: lactoferrin (1,250 and 6,250 nM) and remdesivir (10 nM) as negative controls for 1 h and then infected with SARS-CoV-2 (MOI = 10) for 1 h on ice. Cells were then washed thoroughly with PBS to remove unbound virus and viral RNA was quantified by RT-qPCR. Huh7 were cultured in $NaClO_3$ for 7 d, which strips heparan sulfate proteoglycans from the cell surface, and were subsequently used as a control for lactoferrin mode of action. (*E*) Synergy analysis of lactoferrin in combination with remdesivir. Cells were pretreated with combinations or single agents and infected with SARS-CoV-2 (MOI of 10) for 48 h. Data are shown after normalization to viral control (100%) and represent an average of $n = 3$ biological replicates with $n = 2/3$ technical replicates each. Unpaired *t* tests with Welch's correction were performed in GraphPad Prism to determine significance. $^*P < 0.0001$.

when meeting one of the following criteria: 1) percent infected less than 25% for the median field in at least two concentrations, 2) a dose–response relationship was observed (by inspection) across the five concentrations tested, or 3) reported positive in the literature or were being evaluated in clinical trials for COVID-19.

Dose–Response Analysis in the Confirmation and Combinatorial Screening. Due to the spatial inhomogeneity of infected cells across a single well, approximately half of the fields were undersaturated, resulting in a reproducible distribution per-well. Total cell and infected cell counts were summed over the nine fields, and percent infected cells was averaged over triplicate wells. Cells treated with known fluorescent compounds, including clofazimine, were confirmed to not have spectral interference. Dose–response curves were fit with GraphPad Prism using a semilog four-parameter variable slope model.

Viral Binding Assay. Huh-7 cells were plated in 48-well plates at 100,000 cells per well and allowed to adhere overnight. The following day, compounds were added at the indicated concentration in serum-free DMEM and incubated for 1 h at 4 °C. Following compound incubation, cells were infected with SARS-CoV-2 at an MOI of 10 for 1 h at 4 °C to allow for viral binding. Cells were then washed three times with ice-cold PBS to remove unbound virus, and RNA was extracted by using the Direct-Zol RNA miniprep kit (Zymogen; R2052). Bound virus was then quantified by RT-qPCR (see *Viral Titer Determination*), and percentages were calculated over the infected nontreated condition.

Multicycle Cytopathogenic Effect Reduction Assay. Vero E6 were allowed to adhere overnight in 96-well cell culture plates. A twofold 10-point serial dilution of compounds (5,000 to 5 nM) and SARS-CoV-2 at MOI of 0.002 were added. Cytopathogenic effect (CPE) was evaluated by microscopic scoring at 5 d p.i. The 50% inhibitory concentration (IC_{50}) was calculated by logarithmic interpolation and is defined as the concentration at which the virus-induced CPE is reduced by 50%.

RNAscope of SARS-CoV-2–Infected Cells. PFA-fixed 96-well black plates (Corning; catalog no. 3036) were permeabilized with a step-wise EtOH treatment (25% EtOH for 3 min, 50% EtOH for 3 min, and 70% EtOH overnight at 4 °C). The day after, cells were treated with washing buffer (25% formamide in 1× SSC buffer) for 5 min and hybridized with custom-designed probes targeting positive-sense SARS-CoV-2 RNA directly conjugated with ATTO647 (Ann Arbor Bioscience) at 37 °C overnight in hybridization buffer (dextran sulfate, 25% formamide, and 0.1% SDS). Cells were counterstained with Hoechst 33342 and anti-S protein antibody (Spike antibody 1A9; GeneTex; catalog no. GTX632604) and imaged using a Thermo Fisher CX5 high-content microscope with a 10×/0.45 N.A. LUCPlan FLN objective.

RNA Sequencing and Data Availability. iAEC2 RNA sequencing was performed on the Illumina NovaSeq 6000 system (see *SI Appendix, Supplemental Methods*). The RNA-sequencing data reported in this paper have been deposited in the Gene Expression Omnibus database, https://www.ncbi.nlm.nih.gov/geo (accession no. GSE171390) (64). All other study data are included in the article and/or supporting information.

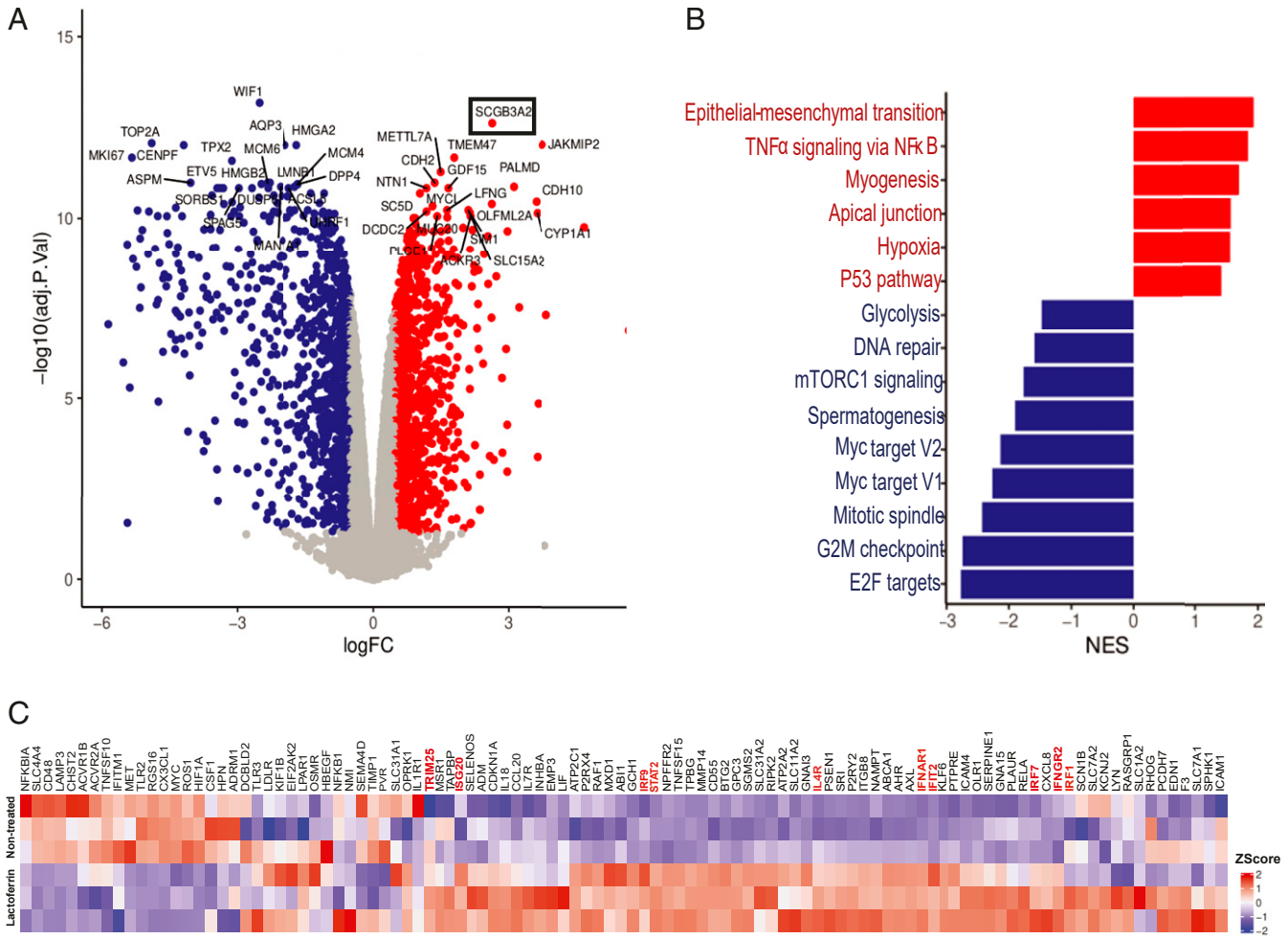

Fig. 7. Lactoferrin indirect antiviral action is mediated by the up-regulation of cellular innate immune response. iAEC2 cells were treated with lactoferrin (6,250 nM) for 48 h, and then RNA was extracted and sequenced. (*A*) Volcano plot of genes down-regulated (blue) and up-regulated (red) upon treatment with lactoferrin. (*B*) Analysis of the top up-regulated and down-regulated pathways. (*C*) Heatmap of selected genes. In red are highlighted genes associated with inflammation and antiviral response.

ACKNOWLEDGMENTS. We acknowledge funding from the University of Michigan Institute for Clinical and Health Research (MICHR) (National Center for Advancing Translational Sciences Grant UL1TR002240) and its Center for Drug Repurposing, and National Cancer Institute Grant P30CA046592 (COVID-19 Administrative Supplement). J.Z.S. is supported by National Institute of Diabetes and Digestive and Kidney Diseases Grant R01DK120623. J.W.W. is supported by the Pharmacological Sciences Training Program T32 Training Grant GM007767. C.M. is supported by Marie-Slodowska Curie individual fellowship (GA-841247) and the MICHR Postdoctoral Translational Scholars Program (Grant UL1TR002240). K.D.A. is supported by the I. M. Rosenzweig Junior Investigator Award from the Pulmonary Fibrosis Foundation. J.R.S. is supported by National Heart, Lung, and Blood Institute Grant R01HL119215, by the National Institute of Allergy and Infectious Diseases Novel Alternative Model Systems for Enteric Diseases Consortium (Grant U19AI116482), and by Grant CZF2019-002440 from the Chan Zuckerberg Initiative Donor-Advised Fund, an advised fund of Silicon Valley Community Foundation. A.M.C. is a Howard Hughes Medical Institute Investigator, an A. Alfred Taubman Scholar, a National Cancer Institute Outstanding Investigator (Grant R35CA231996), and an American Cancer Society Professor. We thank Matthew Chess for Amazon Web Services support, Kevin Jan and Peyton Uhl at Yokogawa for imaging support, Nick Santoro at the University of Michigan Center for Chemical Genomics, and Loren Ward at Glanbia Nutritionals for thoughtful discussions and for providing bulk Bioferrin 2000. We thank David Egan and Wienand Omta from Core Life Analytics for assisting with high-content data analytics, as well as Philip Cheung and Brian Bolt at ReFactor Biosciences for assistance with HTS data registration. We also acknowledge Stephanie Ellison at the Michigan Center for Translational Pathology for assistance with editing and manuscript submission. Finally, we thank Tracey Schultz and Dianne Jazdzyk for project management.

1. F. Xiao *et al.*, Evidence for gastrointestinal infection of SARS-CoV-2. *Gastroenterology* **158**, 1831–1833.e3 (2020).
2. L. Lin *et al.*, Gastrointestinal symptoms of 95 cases with SARS-CoV-2 infection. *Gut* **69**, 997–1001 (2020).
3. A. Avula *et al.*, COVID-19 presenting as stroke. *Brain Behav. Immun.* **87**, 115–119 (2020).
4. A. N. Kochi, A. P. Tagliari, G. B. Forleo, G. M. Fassini, C. Tondo, Cardiac and arrhythmic complications in patients with COVID-19. *J. Cardiovasc. Electrophysiol.* **31**, 1003–1008 (2020).
5. S. Mulangu *et al.*; PALM Writing Group; PALM Consortium Study Team, A randomized, controlled trial of Ebola virus disease therapeutics. *N. Engl. J. Med.* **381**, 2293–2303 (2019).
6. T. I. Oprea *et al.*, Drug repurposing from an academic perspective. *Drug Discov. Today Ther. Strateg.* **8**, 61–69 (2011).
7. L. Riva *et al.*, Discovery of SARS-CoV-2 antiviral drugs through large-scale compound repurposing. *Nature* **586**, 113–119 (2020).
8. M. Dittmar *et al.*, Drug repurposing screens reveal cell-type-specific entry pathways and FDA-approved drugs active against SARS-Cov-2. *Cell Rep.* **35**, 108959 (2021).
9. S. Yuan *et al.*, Discovery of the FDA-approved drugs bexarotene, cetilistat, diiodohydroxyquinoline, and abiraterone as potential COVID-19 treatments with a robust two-tier screening system. *Pharmacol. Res.* **159**, 104960 (2020).
10. C. McQuin *et al.*, CellProfiler 3.0: Next-generation image processing for biology. *PLoS Biol.* **16**, e2005970 (2018).
11. M. Bouhaddou *et al.*, The global phosphorylation landscape of SARS-CoV-2 infection. *Cell* **182**, 685–712.e19 (2020).
12. A. B. Gussow *et al.*, Genomic determinants of pathogenicity in SARS-CoV-2 and other human coronaviruses. *Proc. Natl. Acad. Sci. U.S.A.* **117**, 15193–15199 (2020).

13. W. Chen, X. M. Li, A. L. Li, G. Yang, H. N. Hu, Hepatitis C virus increases free fatty acids absorption and promotes its replication via down-regulating GADD45α expression. *Med. Sci. Monit.* **22**, 2347–2356 (2016).
14. K. Heiser *et al*., Identification of potential treatments for COVID-19 through artificial intelligence-enabled phenomic analysis of human cells infected with SARS-CoV-2. bioRxiv [Preprint] (2020). https://doi.org/10.1101/2020.04.21.054387 (Accessed 3 June 2021).
15. S. Jeon *et al*., Identification of antiviral drug candidates against SARS-CoV-2 from FDA-approved drugs. *Antimicrob. Agents Chemother*., 10.1128/AAC.00819-20 (2020).
16. K. Hurley *et al*., Reconstructed single-cell fate trajectories define lineage plasticity windows during differentiation of human PSC-derived distal lung progenitors. *Cell Stem Cell* **26**, 593–608.e8 (2020).
17. R. J. Mason, Pathogenesis of COVID-19 from a cell biology perspective. *Eur. Respir. J.* **55**, 2000607 (2020).
18. D. B. Kell, E. L. Heyden, E. Pretorius, The biology of lactoferrin, an iron-binding protein that can help defend against viruses and bacteria. *Front. Immunol.* **11**, 1221 (2020).
19. C. T. Meyer *et al*., Quantifying drug combination synergy along potency and efficacy axes. *Cell Syst.* **8**, 97–108.e16 (2019).
20. J. Lang *et al*., Inhibition of SARS pseudovirus cell entry by lactoferrin binding to heparan sulfate proteoglycans. *PLoS One* **6**, e23710 (2011).
21. P. A. Baeuerle, W. B. Huttner, Chlorate—a potent inhibitor of protein sulfation in intact cells. *Biochem. Biophys. Res. Commun.* **141**, 870–877 (1986).
22. T. Siqueiros-Cendón *et al*., Immunomodulatory effects of lactoferrin. *Acta Pharmacol. Sin.* **35**, 557–566 (2014).
23. D. Blanco-Melo *et al*., Imbalanced host response to SARS-CoV-2 drives development of COVID-19. *Cell* **181**, 1036–1045.e9 (2020).
24. K. Li, Z. Chen, N. Kato, M. Gale Jr, S. M. Lemon, Distinct poly(I-C) and virus-activated signaling pathways leading to interferon-beta production in hepatocytes. *J. Biol. Chem.* **280**, 16739–16747 (2005).
25. M. Yoneda *et al*., Secretoglobin superfamily protein SCGB3A2 alleviates house dust mite-induced allergic airway inflammation in mice. *Int. Arch. Allergy Immunol.* **171**, 36–44 (2016).
26. M. K. Mariani *et al*., The combination of IFN β and TNF induces an antiviral and immunoregulatory program via non-canonical pathways involving STAT2 and IRF9. *Cells* **8**, 919 (2019).
27. M. V. Kuleshov *et al*., The COVID-19 drug and gene set library. *Patterns (N Y)* **1**, 100090 (2020).
28. W. Yin *et al*., Structural basis for inhibition of the RNA-dependent RNA polymerase from SARS-CoV-2 by remdesivir. *Science* **368**, 1499–1504 (2020).
29. M. M. Ghahremanpour *et al*., Identification of 14 known drugs as inhibitors of the main protease of SARS-CoV-2. *ACS Med. Chem. Lett.* **11**, 2526–2533 (2020).
30. O. Roscow, R. Ganassin, K. Garver, M. Polinski, Z-FA-FMK demonstrates differential inhibition of aquatic orthoreovirus (PRV), aquareovirus (CSRV), and rhabdovirus (IHNV) replication. *Virus Res.* **244**, 194–198 (2018).
31. X. Ou *et al*., Characterization of spike glycoprotein of SARS-CoV-2 on virus entry and its immune cross-reactivity with SARS-CoV. *Nat. Commun.* **11**, 1620 (2020).
32. A. Pardanani *et al*., TG101209, a small molecule JAK2-selective kinase inhibitor potently inhibits myeloproliferative disorder-associated JAK2V617F and MPLW515L/K mutations. *Leukemia* **21**, 1658–1668 (2007).
33. D. Wu, X. O. Yang, TH17 responses in cytokine storm of COVID-19: An emerging target of JAK2 inhibitor Fedratinib. *J. Microbiol. Immunol. Infect.* **53**, 368–370 (2020).
34. W. Zhang *et al*., The use of anti-inflammatory drugs in the treatment of people with severe coronavirus disease 2019 (COVID-19): The perspectives of clinical immunologists from China. *Clin. Immunol.* **214**, 108393 (2020).
35. J. Stebbing *et al*., COVID-19: Combining antiviral and anti-inflammatory treatments. *Lancet Infect. Dis.* **20**, 400–402 (2020).
36. L. Barrett, Treatment of moderate to severe coronavirus disease (COVID-19) in hospitalized patients. https://clinicaltrials.gov/ct2/show/NCT04321993. Accessed 24 May 2020.
37. Y. Cai, Y. Liu, X. Zhang, Suppression of coronavirus replication by inhibition of the MEK signaling pathway. *J. Virol.* **81**, 446–456 (2007).
38. J. Gu, B. Han, J. Wang, COVID-19: Gastrointestinal manifestations and potential fecal–oral transmission. *Gastroenterology* **158**, 1518–1519 (2020).
39. S. Yuan *et al*., Clofazimine broadly inhibits coronaviruses including SARS-CoV-2. *Nature* **593**, 418–423 (2021).
40. R. Reghunathan *et al*., Expression profile of immune response genes in patients with severe acute respiratory syndrome. *BMC Immunol.* **6**, 2 (2005).
41. C. Han *et al*., Digestive symptoms in COVID-19 patients with mild disease severity: Clinical presentation, stool viral RNA testing, and outcomes. *Am. J. Gastroenterol.* **115**, 916–923 (2020).
42. H. Oda *et al*., Antiviral effects of bovine lactoferrin on human norovirus. *Biochem. Cell Biol.* **99**, 166–172 (2021).
43. A. Cutone *et al*., Lactoferrin prevents LPS-induced decrease of the iron exporter ferroportin in human monocytes/macrophages. *Biometals* **27**, 807–813 (2014).
44. P. Conti *et al*., Induction of pro-inflammatory cytokines (IL-1 and IL-6) and lung inflammation by coronavirus-19 (COVI-19 or SARS-CoV-2): Anti-inflammatory strategies. *J. Biol. Regul. Homeost. Agents* **34**, 327–331 (2020).
45. F. A. Lagunas-Rangel, V. Chávez-Valencia, High IL-6/IFN-γ ratio could be associated with severe disease in COVID-19 patients. *J. Med. Virol.* **92**, 1789–1790 (2020).
46. I. F.-N. Hung *et al*., Triple combination of interferon beta-1b, lopinavir-ritonavir, and ribavirin in the treatment of patients admitted to hospital with COVID-19: An open-label, randomised, phase 2 trial. *Lancet* **395**, 1695–1704 (2020).
47. A. Jacob *et al*., Derivation of self-renewing lung alveolar epithelial type II cells from human pluripotent stem cells. *Nat. Protocols* **14**, 3303–3332 (2019).
48. M. R. Berthold *et al*., KNIME—the Konstanz information miner. *SIGKDD Explor.* **11**, 26–31 (2009).
49. J.-L. R. Stevens, P. Rudiger, J. A. Bednar, "HoloViews: Building complex visualizations easily for reproducible science" in *Proceedings of the 14th Python in Science Conference* (SciPy, 2015), pp. 61–69.
50. C. I. Haffajee *et al*., Clinical pharmacokinetics and efficacy of amiodarone for refractory tachyarrhythmias. *Circulation* **67**, 1347–1355 (1983).
51. Pfizer Inc., Bosutinib (package insert) (Pfizer Inc., 2017).
52. P. C. Feng, C. C. Fenselau, R. R. Jacobson, Metabolism of clofazimine in leprosy patients. *Drug Metab. Dispos.* **9**, 521–524 (1981).
53. Y. C. Huang, J. L. Colaizzi, R. H. Bierman, R. Woestenborghs, J. J. Heykants, Pharmacokinetics and dose proportionality of domperidone in healthy volunteers. *J. Clin. Pharmacol.* **26**, 628–632 (1986).
54. Bristol-Myers Squibb Company, Entecavir (package insert) (Bristol-Myers Squibb Company, 2010).
55. Celgene Corporation, Fedratinib (package insert) (Celgene Corporation, 2019).
56. Astellas Pharma US Inc., Gilteritinib (package insert) (Astellas Pharma US Inc., 2019).
57. Aegerion Pharmaceuticals, Inc., Lomitapide (package insert) (Aegerion Pharmaceuticals Inc., 2012).
58. ANI Pharmaceuticals Inc., Metoclopramide (package insert) (ANI Pharmaceuticals Inc., 2017).
59. S. Burock *et al*., Phase II trial to investigate the safety and efficacy of orally applied niclosamide in patients with metachronous or sychronous metastases of a colorectal cancer progressing after therapy: The NIKOLO trial. *BMC Cancer* **18**, 297 (2018).
60. Gilead Sciences Inc., Remdesivir (package insert) (Gilead Sciences Inc., 2020).
61. J. Täubel *et al*., Single doses up to 800 mg of E-52862 do not prolong the QTc interval–A retrospective validation by pharmacokinetic-pharmacodynamic modelling of electrocardiography data utilising the effects of a meal on QTc to demonstrate ECG assay sensitivity. *PLoS One* **10**, e0136369 (2015).
62. D. L. Lancaster, N. Patel, L. Lennard, J. S. Lilleyman, 6-Thioguanine in children with acute lymphoblastic leukaemia: Influence of food on parent drug pharmacokinetics and 6-thioguanine nucleotide concentrations. *Br. J. Clin. Pharmacol.* **51**, 531–539 (2001).
63. Pfizer Inc., Verapamil (package insert) (Pfizer Inc., 2017).
64. C. Mirabelli *et al*., Effect of lactoferrin treatment on iAEC2. Gene Expression Omnibus. https://www.ncbi.nlm.nih.gov/geo/query/acc.cgi?acc=GSE171390. Deposited 2 April 2021.